Published in *Materials Chemistry and Physics*, 2021

Molecular Dynamics Modeling of Mechanical and Tribological Properties of Additively Manufactured AlCoCrFe High Entropy Alloy Coating on Aluminum Substrate

Xuehui Yang[1], Jian Zhang[1], Sugrim Sagar[1], Tejesh Dube[1], Bong-Gu Kim[2], Yeon-Gil Jung[2], Dan Daehyun Koo[3], Alan Jones[1], Jing Zhang[1*]

1. Department of Mechanical and Energy Engineering, Indiana University–Purdue University Indianapolis, Indianapolis, Indiana, USA

2. Department of Materials Convergence and System Engineering, Changwon National University, Republic of Korea

3. Department of Engineering Technology, Indiana University–Purdue University Indianapolis, Indianapolis, Indiana, USA

*Corresponding author: jz29@iupui.edu

Abstract

In this work, an improved molecular dynamics (MD) model is developed to simulate the nanoindentation and tribological tests of additively manufactured high entropy alloys (HEA) AlCoCrFe coated on an aluminum substrate. The model shows that in the interface region between the HEA coating and Al substrate, as the laser heating temperature increases during the HEA coating additive manufacturing process, more Al in the substrate is melted to react with other elements in the coating layer, which is qualitatively in agreement with experiment in literature. Using the simulated nanoindentation tests, the calculated Young's modulus of pure Al and Al with HEA coating is 79.93 GPa and 119.30 GPa, respectively. In both our simulations and the experimental results in the literature, the hardness of Al with the HEA coating layer is about 10 times higher than the Al hardness, indicating that HEA can significantly improve the hardness of the metallic substrate. Using the simulated tribological scratch tests, the computed wear tracks are

qualitatively in agreement with experimental images in literature. Both our model and experiment show that the Al with HEA coating has a much smaller wear track than that of Al, due to less plastic deformation, confirmed by a dislocation analysis. The computed average coefficient of friction of Al is 0.62 and Al with HEA coating is 0.14. This work demonstrates that the HEA coating significantly improves the mechanical and tribology properties, which are in excellent agreement with the experiments reported in the literature.

Keywords: High entropy alloy; molecular dynamics; nanoindentation; scratch test; mechanical property; tribological property

1. Introduction

High entropy alloys (HEA) are single-phase-disordered solid solution alloys with four or more principal elements with their concentrations between 5%-35% by elements definition [1, 2]. HEAs are the alloys that have entropy larger than 1.5R by entropy definition, where R is the gas constant. As HEAs have multi principal elements, they can take advantage of tunable properties because of large material compositional space, including high hardness, strength, and ductility, oxidation and wear resistance, and magnetism, etc. [3]. Intermetallic phases HEAs such as AlCoCrFeNiTi have shown high yield strength and hardness[4, 5], which can be potentially used for aerospace applications. Senkov[6] studied two refractory high entropy alloys $Nb_{25}Mo_{25}Ta_{25}W_{25}$ and $V_{20}Nb_{20}Mo_{20}Ta_{20}W_{20}$ due to their good high-temperature mechanical properties and thermal protection applications. Youssef[7] synthesized a nanocrystalline high entropy alloy $Al_{20}Li_{20}Mg_{10}Sc_{20}$, which showed relatively high mechanical hardness and high strength-to-weight ratio. $Al_{0.5}$CoCrCuFeNi demonstrated better fatigue behaviors than several conventional alloys under relatively high stress conditions[8]. Additionally, some HEAs showed good corrosion resistance. For example, $FeCoNiCrCu_x$ showed a better corrosion resistance than 304L stainless steel in NaCl [9] and H_2SO_4 solutions[10].

To further improve the performance of the metallic substrate, HEA coatings have been applied to metallic substrates to enhance their surface properties, for example, to minimize tribocorrosion issues. Huang[11] fabricated the TiVCrAlSi HEA coatings on Ti6Al4V substrate to improve its wear resistance. Zhang[12] synthesized FeCoCrAlNi HEA coating on 304 stainless steel to improve its corrosion and cavitation erosion resistance. FeNiCoAlCu HEA coating[13] showed a good wear performance under high temperatures due to the formation of oxide film on the surface. In Ref. [14], laser-based additively processed Al–Co–Cr–Fe HEA coatings on aluminum were studied. The experimental results showed good mechanical and tribology properties of the additively manufactured HEA coatings[14].

Although numerous experimental studies as discussed above, however, due to large numbers of combinations of HEA compositions, it is prohibitive to use experimental methods alone to fully understand new HEA systems. Therefore, the modeling approach is employed to simulate the multi-component alloy systems, which makes it more efficient to design desirable HEAs [15, 16]. Ikeda conducted a review on the *ab initio* study of phase stabilities and mechanical properties of

multicomponent alloys [17]. Choi investigated the effect of individual elements on solid solution hardening for equiatomic CoCrFeMnNi HEA based on atomistic simulations using Monte Carlo, molecular dynamics, and molecular statics methods[18]. Zhang used the CALPHAD (CALculation of PHAse Diagrams) approach to calculate binary and multicomponent phase diagrams[19].

In this work, an improved molecular dynamics model is developed to simulate the additively processed HEA coatings deposited on an aluminum substrate. The coating fabrication process, nanoindentation test, and scratch test are simulated, to understand the mechanical and tribology properties and the associated structure and phase changes. Selected simulation results are also compared against the experimental observations reported in Ref. [14].

2. Model details

2.1 Molecular dynamics models

In this work, a molecular dynamics model of AlCoCrFe HEA coating deposited on an aluminum substrate was constructed. For the AlCoCrFe HEA coating, randomly distributed atoms were positioned using the BCC structure and equal composition with a lattice parameter of 2.878Å. For the Al substrate, the structure was built based on the FCC lattice structure with the lattice parameter of 4.0502Å. The crystal orientations for both layers are <100>. The model assumes periodic boundary conditions along the X and Y axes and a non-periodic and shrink-wrapped boundary condition along the Z-axis. The model size is 143.9Å×287.8Å×124.2Å, and the total number of atoms is 337,104. Large-scale Atomic/Molecular Massively Parallel Simulator (LAMMPS)[20] was used to compute the MD model.

First, the energy of the whole structure was minimized using the conjugate gradient (CG) algorithm. Then to simulate the HEA coating fabrication process, the HEA coating layer was formed through a heating-cooling process. The HEA coating layer was heated from room temperature to the selected temperature (1,000 ~1,500K) in 50,000 fs. Then, the temperature was held at the selected temperature for 100,000 fs. The HEA coating layer was cooled down to room temperature in 50,000 fs, and the temperature was kept at room temperature for 50,000fs. The temperature of the Al substrate was kept at room temperature for all the steps. The timestep is 1.0 fs. During the

simulation of the nanoindentation and tribological scratch tests, the bottom atom layer was fixed to prevent rigid body motion. A spherical indenter with a radius of 30 Å was used in the nanoindentation and tribological scratch tests.

2.2 EAM interatomic potential formulation

The embedded atom method (EAM) potential includes two parts and can be expressed as [21]:

$$E_i = F_\alpha\left(\sum_{j\neq i}\rho_\beta(r_{ij})\right) + \frac{1}{2}\sum_{j\neq i}\phi_{\alpha\beta}(r_{ij}) \quad (1)$$

where F is the embedding energy, ρ is local electronic density, and ϕ is pair-wise interaction force. Both summations in the formula are calculated when the atom i and j in the cutoff distance. The EAM potentials for elements (Al, Co, Fe, Ni, and Ti) were taken from Zhou's work [22], and the interatomic potentials of Cr were taken from Anand's paper [23], which used a similar parameter system as Zhou's work [22]. In this work, the parameters of Cr[24] (as shown in Table 1) were added to the Zhou's potential, and then Al, Co, Cr, and Fe were chosen in the Zhou EAM input file. A revised new potential of HEA AlCoCrFe was completely formulated.

Table 1 Parameters of the EAM potential for Cr [24]

r_e(Å)	$f_e(eV/Å)$	$p_e(eV/Å)$	$p_s(eV/Å)$	κ	λ	$A(eV)$	$B(eV)$	α	β
2.493 879	1.793 835	17.641 302	19.605 45	0.185 33	0.277 995	1.551 848	1.827 556	8.604 593	7.170 494
$F_o(eV)$	$F_1(eV)$	$F_2(eV)$	$F_3(eV)$	η	$F_{mo}(eV)$	$F_{m1}(eV)$	$F_{m2}(eV)$	$F_{m3}(eV)$	$F_n(eV)$
-2.022 754	0.039 608	-0.183 611	-2.245 972	0.456	−2.02	0	-0.056 517	0.439 144	-2.020 038

2.3 Calculation of the Young's modulus in the nanoindentation test

To predict the Young's modulus, the nanoindentation model with a spherical indenter was chosen in this work. The equations used for the Hertzian force-displacement are [25]:

$$F = \frac{4}{3}E^* R^{1/2} d^{3/2} \quad (2)$$

$$\frac{1}{E^*} = \frac{1-\nu_1^2}{E_1} + \frac{1-\nu_2^2}{E_2} \quad (3)$$

where F is the load, d is the depth inside the sample. R is the spherical indenter radius. E_1 are ν_1 are the Young's modulus and Poisson's ratio of the sample, respectively. E_2 and ν_2 are the Young's modulus and Poisson's ratio of the indenter, respectively.

In this model, the indenter is assumed to be rigid and therefore E_2 is infinite. Thus, the Young's modulus can be calculated as:

$$E_1 = (1 - \nu_1^2)E^* \tag{4}$$

2.4 Calculation of hardness

The hardness in the nanoindentation can be defined as [26]:

$$H = \frac{P_{max}}{A_c} \tag{5}$$

$$h_c = h_{max} - \varepsilon \frac{P_{max}}{S} \tag{6}$$

$$A_c = \frac{\pi d_c^2}{4} \tag{7}$$

where P_{max} is the maximum indentation load, A_c is the projected contact area under the peak indentation depth, h_c is used to calculate the projected contact area determined by Sneddon's equation, and ε is a geometric constant and equals to 0.75 for a spherical indenter, and $d_c$is the diameter of the residual impression on the surface. S is the contact stiffness by the fitting of the unloading force-displacement curve.

2.5 Calculation of volume loss due to wear

To calculate the volume loss due to wear, the OVITO tool construct surface mesh[27] was used to construct the surface representation. The inner and outer boundaries of the atomic solid can be identified with the surface mesh. The alpha-shape algorithm method was chosen and the option of the identification of volumetric regions was selected.

3. Results and discussions

3.1 Validation of the AlCoCrFe EAM potential

The proposed AlCoCrFe EAM potential was validated by calculating the lattice parameter. AlCoCrFe potential validation model was built with randomly distributed atoms and equal composition. The boundary conditions are periodic. The validation model was first heated over the melting temperature then cool down to room temperature. The lattice parameter was calculated after the heating-cooling process. The calculated lattice parameter using the proposed AlCoCrFe EAM potential is 2.878Å, which is in excellent agreement with the experimental value 2.878Å reported in Ref. [28].

3.2 Analysis of structure transformations at the interface

As shown in Figure 1, the crystal structure of the interface after the heating-cooling process are studied. The OVITO tool common neighbor analysis (CNA)[27] with a variable cutoff was used to identify the crystal structures, as shown in Figure 1. The crystal structure of the Al substrate is FCC, while AlCoCrFe HEA coating is BCC. The interface region between the HEA coating and Al substrate was isolated as a slab with a thickness of 20Å (Figure 1).

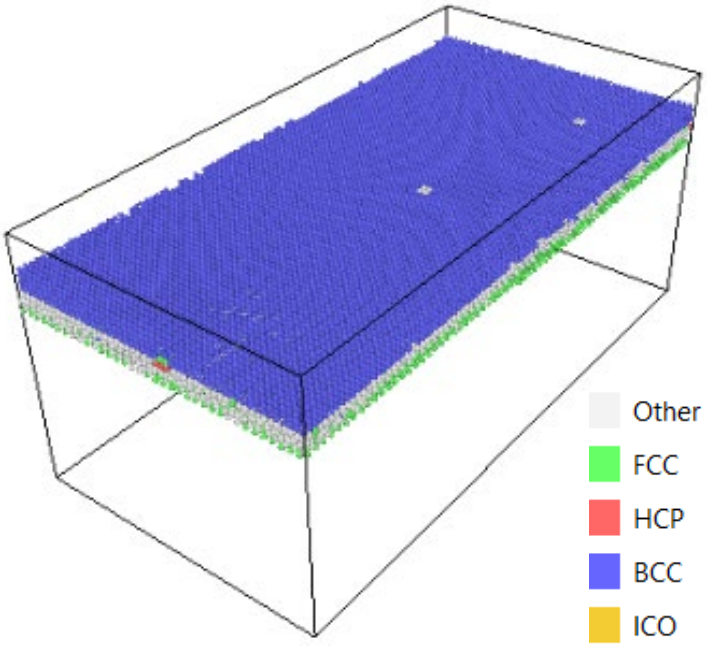

Figure 1: Crystal structures of the interface region between the HEA coating and Al substrate. FCC - face-centered cubic, BCC -body-centered cubic, HCP- hexagonal closed-packed, and ICO – icosahedral.

In the interface region, the fractions of the BCC structure and other structures were computed as summarized in Figure 2. As shown in the figure, as the laser heating temperature increases during the HEA coating additive manufacturing process, more Al in the substrate is melted to react with other elements in the coating layer. Therefore, less BCC structure and more other structures are formed. Since our HEA and aluminum layers have a crystal orientation of <100>, which is different from the crystal orientations of either NW or KS interfaces, so we don't observe these two structures in our system.

Our modeling result has a similar trend with the experimental observation in Ref. [14] in the inset of Figure 2. As discussed in Ref. [14], the increase of laser heat input during the additive manufacturing process leads to the structural change of the HEA phase. Also, the increase of heating and cooling rates results in the formation of several intermetallic phases Al_3Fe, Al_9Co_2, and $Al_{13}Co_4$. Both our modeling results and experimental observation suggest that the laser heating temperature shouldn't be too high in order to avoid excessive lose of the HEA phases.

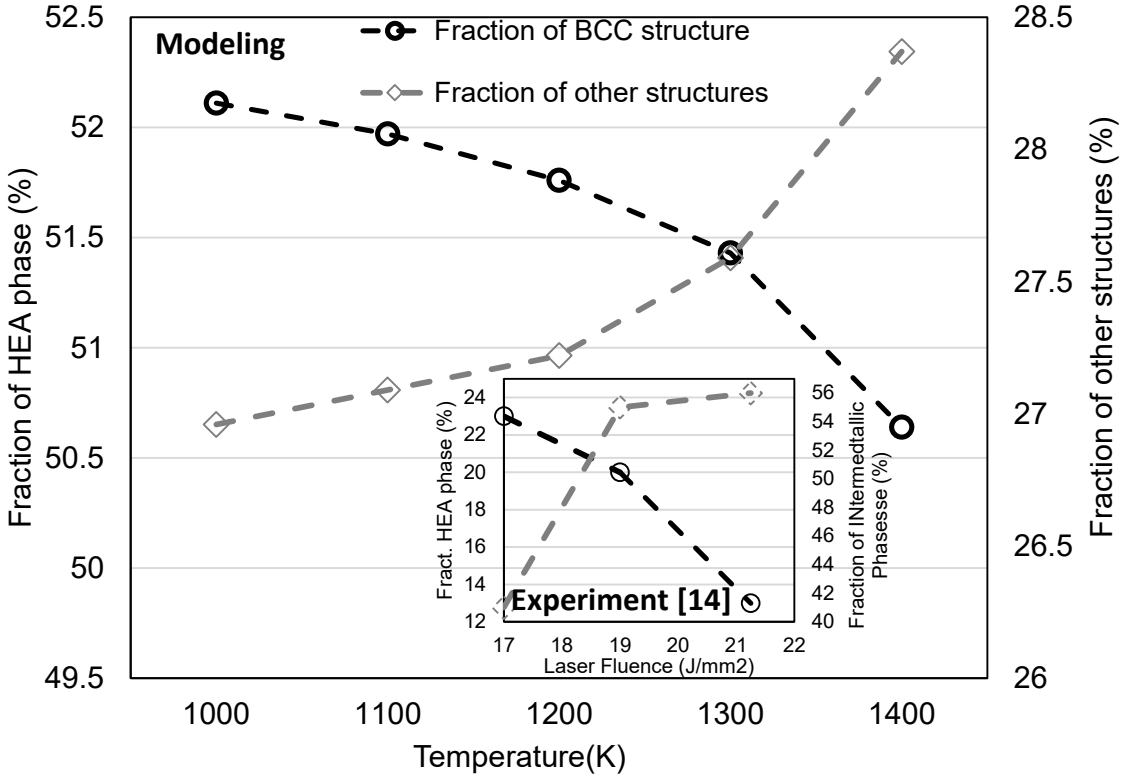

Figure 2: Simulated phase fractions of HEA and other structures in the interface region, as a function of heating temperature. It shows a similar trend as the experimental measurements (inset) in Ref.[14].

3.3 Analysis of nanoindentation mechanical properties

Figure 3 shows the force vs. depth curves for a cycle of nanoindentation and indenter retraction for both the pure Al (Figure 3a) and HEA coated Al (Figure 3b) models. Comparing the two figures, the indentation depth of pure Al is approximate 28 Å, which is much larger than about 9 Å of the HEA coated Al under the same indentation force. After retraction, approximately 20 Å depth plastic deformation remains on Al, while only 2 Å for Al with HEA coating. The results indicate that HEA coating can significantly improve the hardness of the metallic substrate.

The Hertzian fitting presented in Equation 5 was used on the unloading curve to calculate the Young's modulus. The Young's modulus of pure Al and Al with HEA coating is 79.93 GPa and 119.30 GPa, respectively. The Young's modulus of Al with HEA coating is larger than that of pure Al, suggesting that HEA coated Al is much stiffer than pure Al.

With the calculated Young's modulus, the computed hardness values for pure Al and Al with HEA coating are 7.25 GPa and 79.58 GPa, respectively. The experimental hardness of Al is 30HV, which corresponds to 0.29 GPa, and the hardness values of Al with HEA coating are between 270HV and 500HV [14], which correspond to 2.65GPa to 4.9 GPa. In both our simulations and experimental results in Ref. [14], the hardness of Al with the HEA coating layer is about 10 times higher than the Al hardness, indicating that HEA can significantly improve the hardness of the metallic substrate.

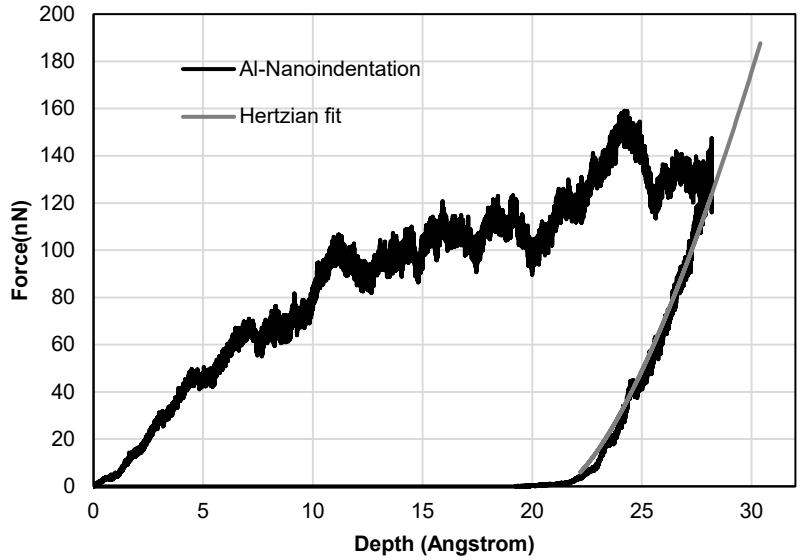

(a)

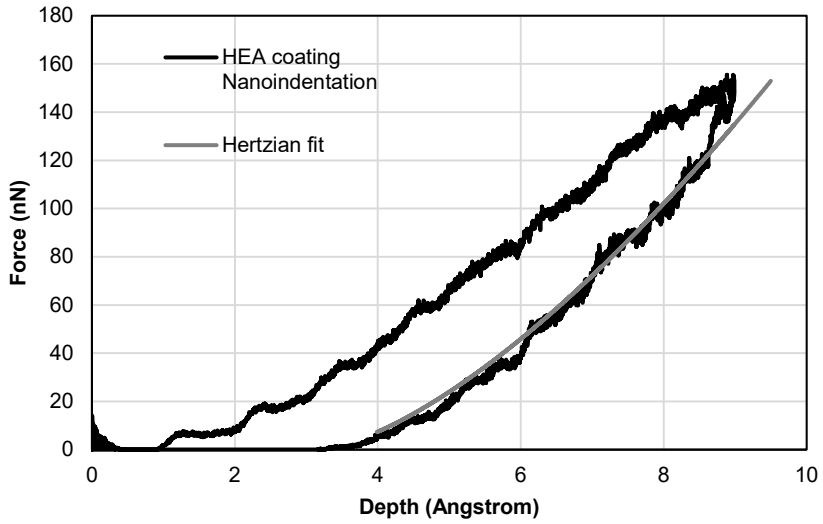

(b)

Figure 3: Simulated force vs. nanoindentation depth curves of (a) pure Al, and (b) Al with HEA

The deformations of the pure Al and HEA coated Al are visualized using OVITO[27] as shown in Figure 4, for both at the maximum indentation depth and after indenter retraction. During the nanoindentation tests, the atoms were compressed by the indenter and the potential energy of deformed atoms was increased, which is colored in the figure.

For pure Al, Figure 4(a-c) show the deformations of Al at the maximum indentation depth, and Figure 4(d-f) are the deformations after the retraction process. In addition to the indentation mark directly caused by the indenter, there are also some deformed atoms on the surface, which are extruded over the surface. After the retraction process, the projected area in the indentation mark is decreased because of the elastic deformation recovery.

In comparison, for the HEA coated Al model, Figure 4 shows the deformation at the maximum indentation depth (Figure 4(g-i)) and after the retraction process (Figure 4(j-l)). The maximum indentation mark diameter for Al (Figure 4a) is about 68Å, while the Al with HEA coating is only about 25Å (Figure 4g), indicating a higher hardness for the HEA coating than pure Al.

Moreover, the surface of the Al with HEA coating (Figure 4h) is much smoother than pure Al (Figure 4b), with fewer atoms protruded on the surface during the nanoindentation test. A similar trend is observed after the retraction process. The observed difference between the pure Al and HEA coated Al models is due to the high Young's modulus and hardness of the HEA layer.

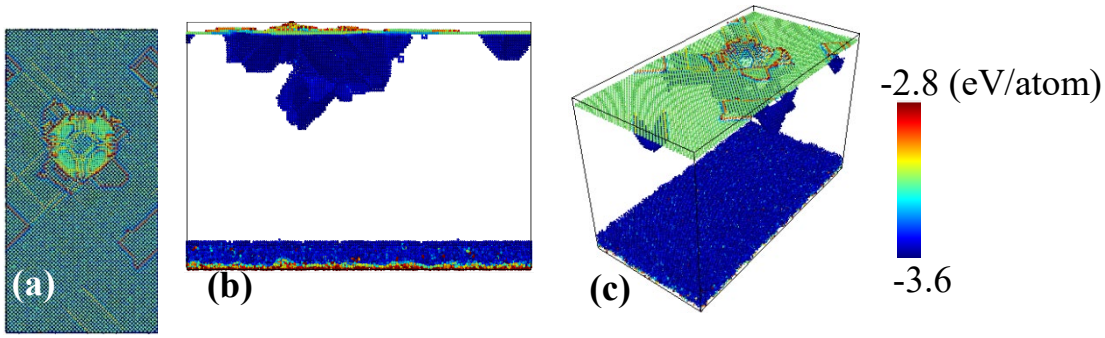

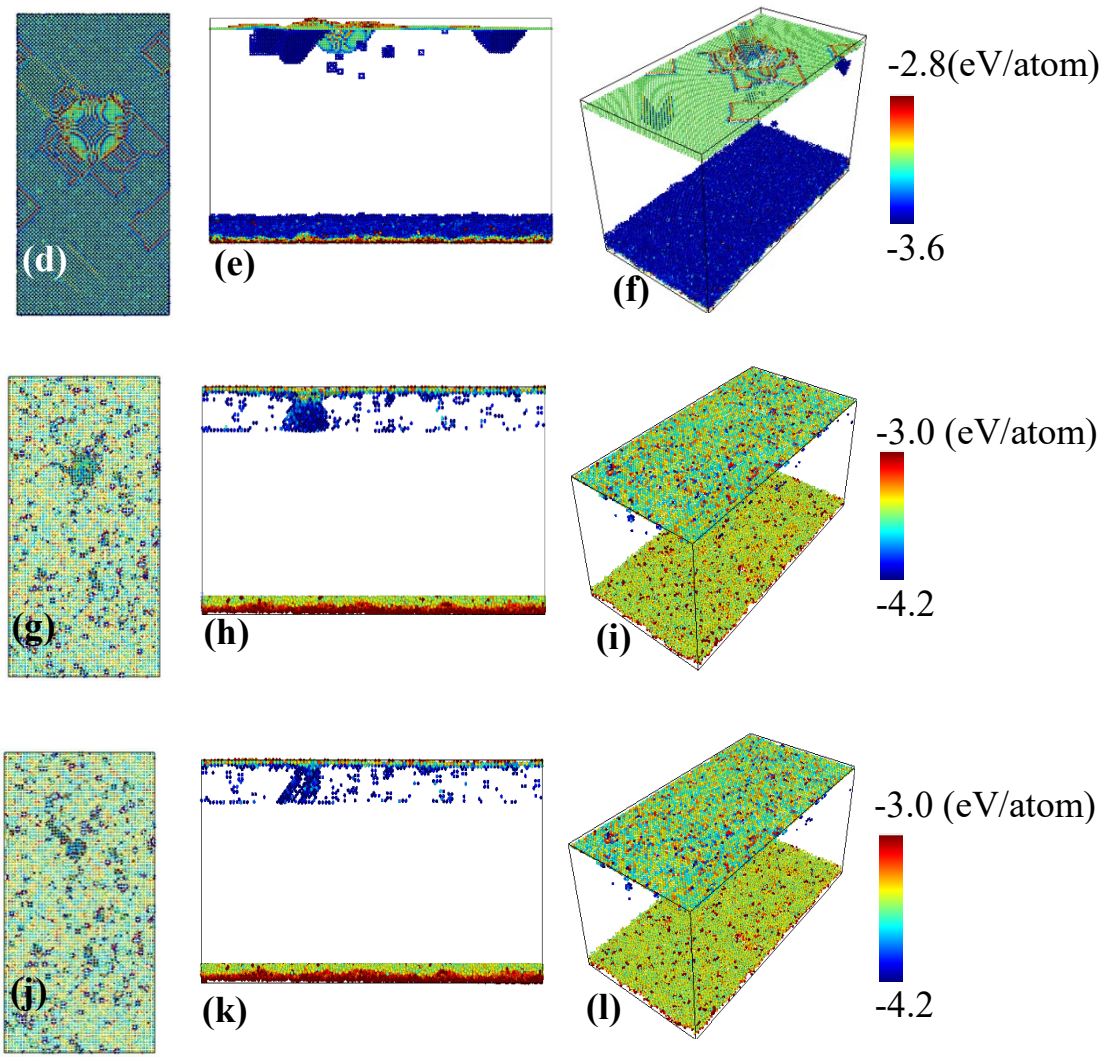

Figure 4: Simulated deformations at either the maximum nanoindentation depth or after the indenter retraction. The left figures (a, d, g, and j) are the top views, middle figures (b, e, h, and k) are the side views, and right figures (c, f, i, and l) are the 3D views. (a-c) Pure Al at maximum indentation depth; (d-f) pure Al after retraction; (g-i) HEA coated Al at maximum indentation depth; and (j-l) HEA coated Al after retraction. The atoms are colored according to the potential energy per atom.

Figure 5 and Figure 6 show the stress distribution along with z-direction and shear strain distribution of pure Al and HEA coated Al, at the maximum indentation depth and after indenter retraction, respectively. The stress distribution was colored by the per-atom stress tensor along the z-direction. The shear strain was measured by OVITO tool atomic strain[27]. From Figure 5(a)

and Figure 6(a, b) the stress is maximum at the area of indentation area, while there is still some stress below the indentation area and the stress shows slightly radial. The strain distribution also shows a similar trend with a more obvious radial distribution, which indicates that some cracks were generated below the indentation area. After retraction (Figure 5(b) and Figure 6(c, d)), the stress and deformed area decrease. The residual stress is caused by plastic deformation after retraction. The radial distribution of stress disappears, but the strain distribution is still radial around the indentation area, which represents the existence of cracks. From Figure 5(c), the maximum stress is larger than that of pure Al. There is some stress at the whole interface between HEA coating and Al substrate layers and uniformly distributed at the Al substrate below the indentation area. Figure 6 (e, f) shows that the strain is smaller than that of pure Al. There is some strain at the interface. After retraction (Figure 5(d) and Figure 6 (g, h)), the stress and strain at the Al substrate and the stress at the indentation area and interface decrease. By comparing, HEA coated Al has higher maximum stress and smaller maximum strain. HEA coating can prevent the generation of cracks during the nanoindentation test.

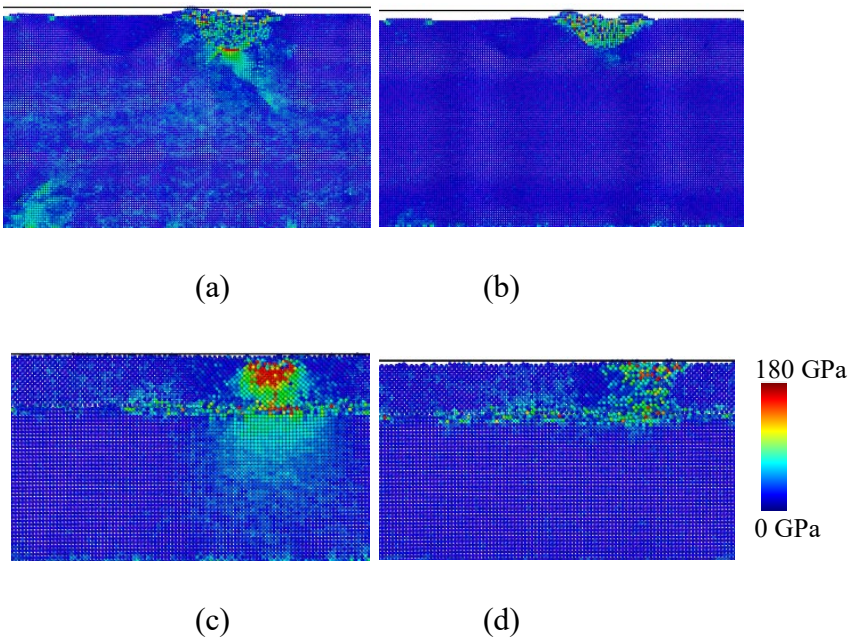

Figure 5: Stress distributions along with z-direction. (a) Al at maximum indentation; (b) Al after indenter retraction; (c) HEA coated Al at maximum indentation depth; and (d) HEA coated Al after indenter retraction

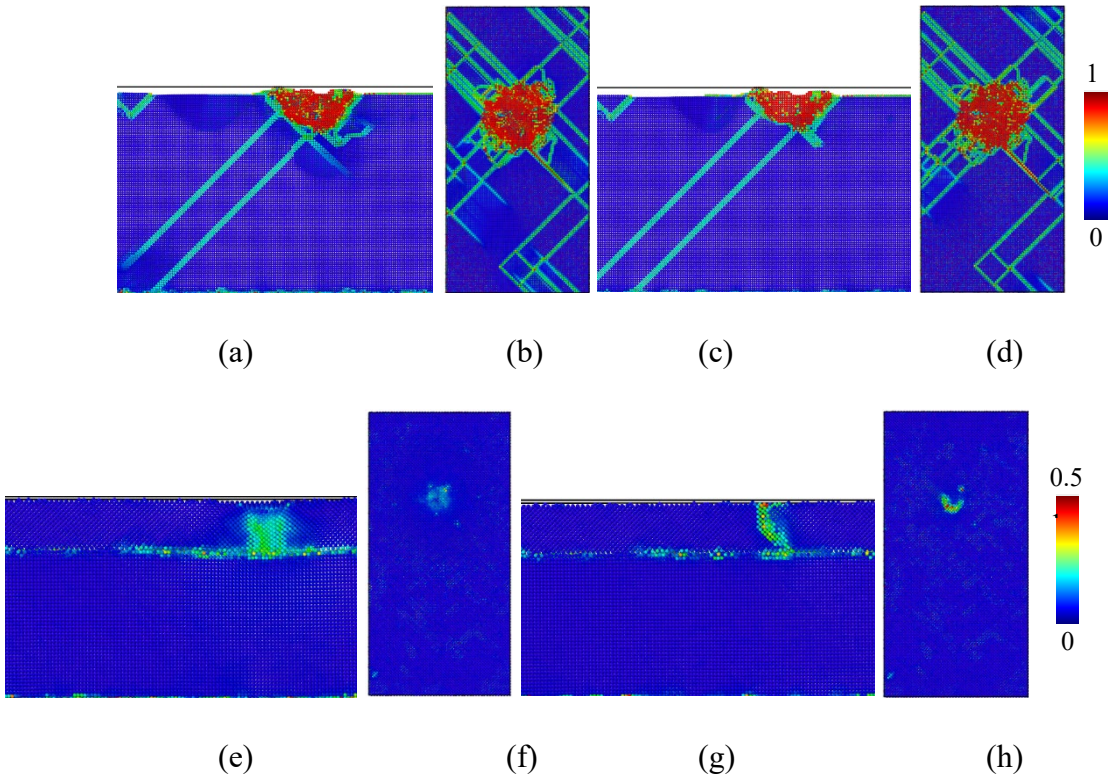

Figure 6: Shear strain distributions. (a, b) Al at maximum indentation; (c, d) Al after indenter retraction; (e, f) HEA coated Al at maximum indentation depth; and (g, h) HEA coated Al after indenter retraction

3.4 Analysis of tribological properties

Scratch tests with the same normal force were simulated to understand the tribology properties. The simulated wear tracks after the scratch tests are compared against the optical interferograms of the experimental tribo-corrosion wear tracks [14], as shown in Figure 7. The simulated wear track of Al is about 60 Å in width and 28 Å in-depth, while the Al with HEA coating is much shallow, with 21 Å in width and 6 Å in depth.

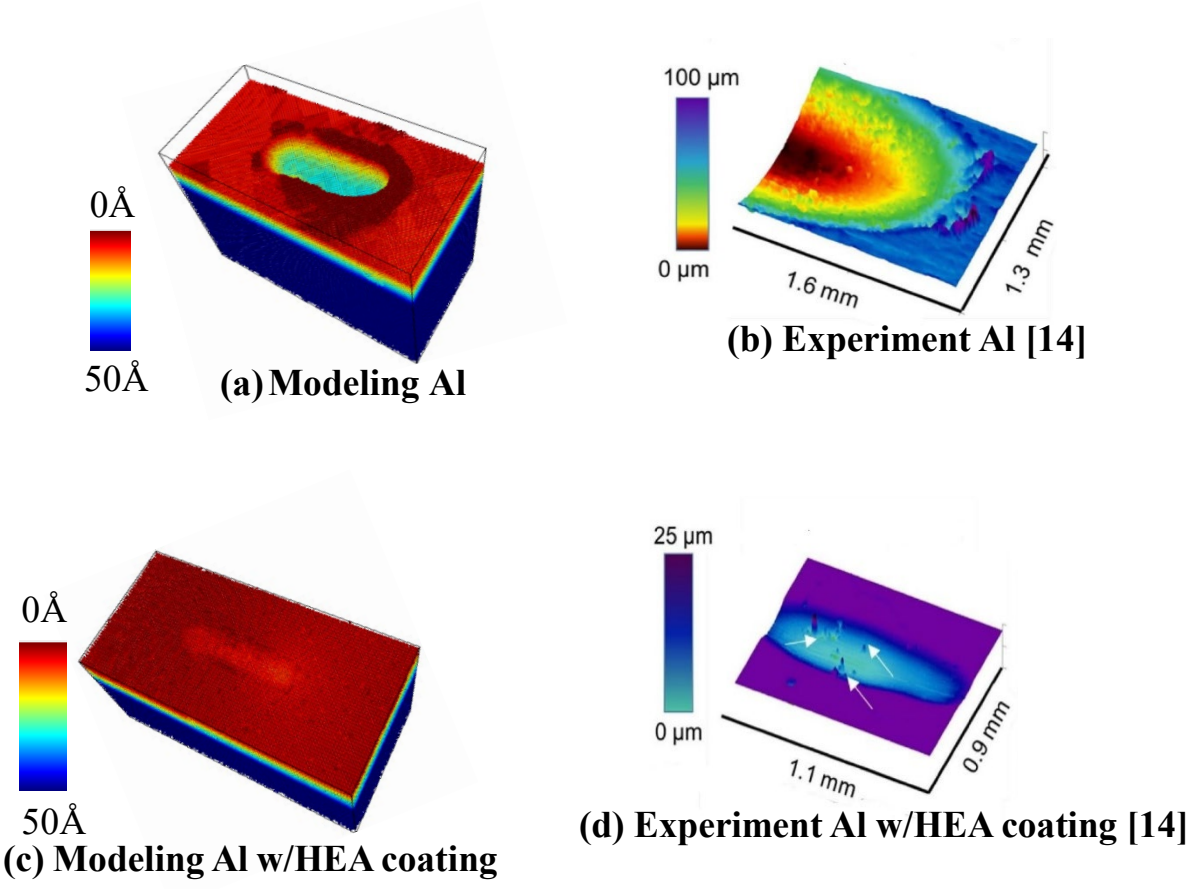

Figure 7: Comparison of the simulated wear tracks of Al and Al with HEA coating with experiments [14]. (a) Simulated wear track of Al, (b)experimental wear track of Al, (c)simulated wear track of Al with HEA coating, and (d)experimental wear track of Al with HEA coating.

The simulation results are qualitatively in agreement with the experimental images [14]. Both the simulation and experiment show that the width and depth of the Al track are about four times that of Al with HEA coating, suggesting that the HEA coating provides an excellent wear resistance of the Al substrate.

Additionally, the wear volume losses of the Al and Al with HEA coating were calculated with OVITO tool construct surface mesh (Figure 8), and which are 1.25e+06 $Å^3$ and 9.95e+05 $Å^3$, respectively. It is noted that the HEA coating protects the Al substrate, reducing the wear loss by about 12 times, compared to the pure Al. The modeling results are qualitatively in good agreement with the experimental measurement in Ref. [14], in which the experimental wear loss of the Al is 0.11 mm^3 and the Al with HEA coating is in the range of 0.01-0.03 mm^3 [14]. Both our model and

the experimental observation in Ref. [14] show that HEA coating provides an excellent wear resistance of the Al substrate.

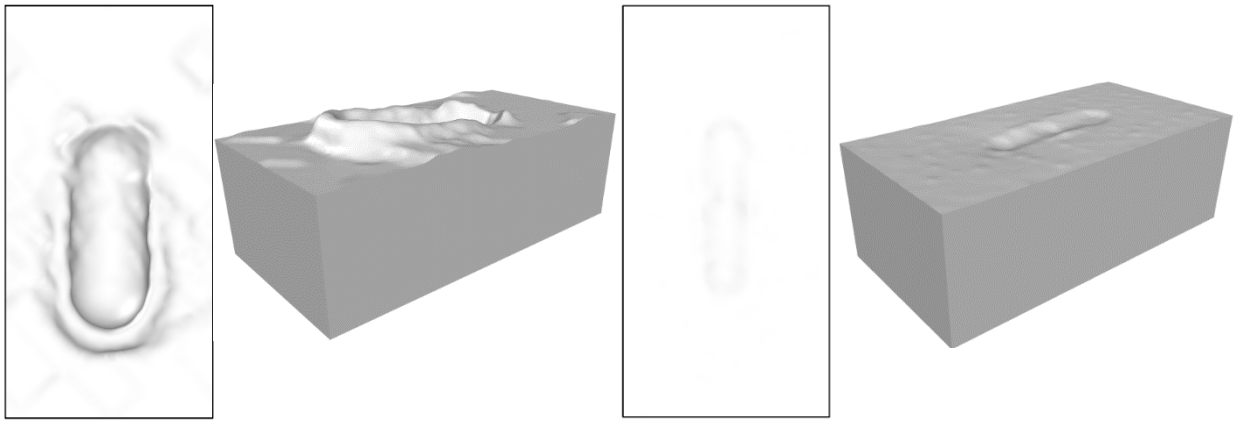

Figure 8 Simulated surface outline of the wear track after the scratch test. (a)Al top view, (b)Al total view, (c) Al with HEA coating top view, and (d) Al with HEA coating total view.

To understand the plastic deformation process in the scratch test, dislocation analysis was conducted on the simulated wear tracks, as shown in Figure 9. For pure Al in Figure 9(a), multiple dislocations are seen on the left side where the indenter was applied at the end of the scratch test. The total length of the dislocations in Al is 3,073.79Å, while only 66.76Å for the Al with HEA coating is shown in Figure 9(b). Therefore, more plastic deformations occurred in the pure Al than the HEA coated Al. This is also related to the observed wear tracks and wear volume losses in Figure 7. It is concluded that the HEA coated Al has a better wear-resistance performance than pure Al alone.

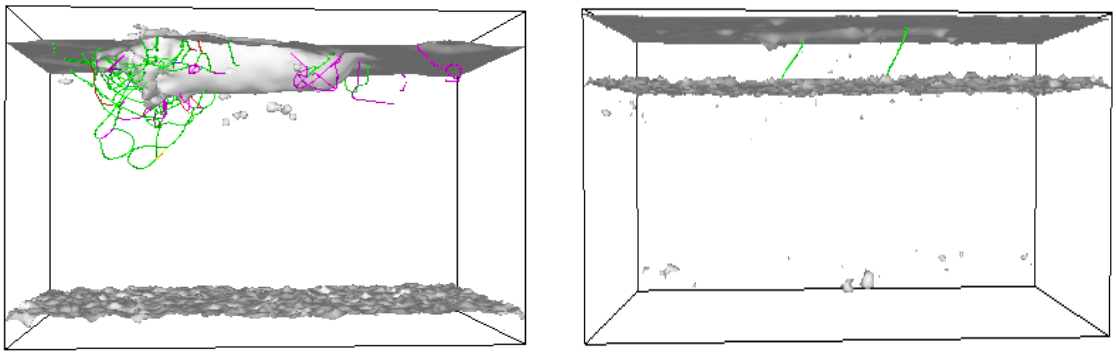

(a) **(b)**

Figure 9: Simulated dislocations after the scratch test. The scratch tests were conducted from the right side to the left side. (a)Al, and (b) Al with HEA coating

The coefficients of friction during the scratch test are further analyzed. Figure 10(a) and (c) show the evolutions of the normal and lateral forces for the Al and HEA coated Al, respectively. The coefficient of friction is computed using the ratio of the lateral to normal forces. Figure 10(b)(d) shows the evolutions of the coefficients of friction during the scratch test.

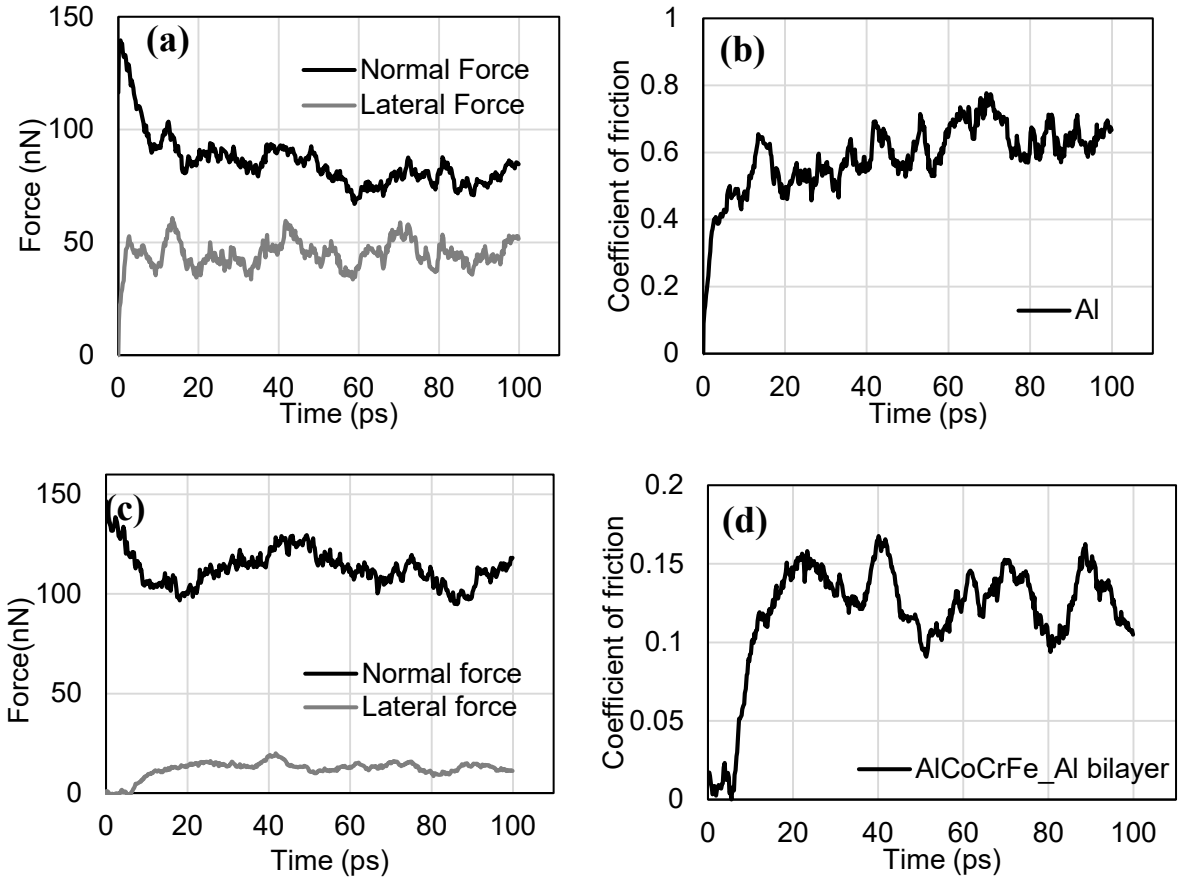

Figure 10: Simulated force and coefficient of friction evolutions during the scratch tests. (a) Force vs. time of Al, (b) coefficient of friction vs. time of Al, (c) forces vs. time of Al with HEA coating, and (d) coefficient of friction vs. time of Al with HEA coating.

Comparing Figure 10(a) and Figure 10(c), both the normal and lateral forces reach a stable stage after 10 ps. The normal force in the HEA coated Al is higher than pure Al, while the lateral force is much lower, due to the high Young's modulus of the HEA coating.

As shown in Figure 10(b) and Figure 10(d), the coefficient of friction, the average coefficient of friction of Al is approximately 0.62, while Al with HEA coating is only about 0.14, or five times less than Al. As analyzed in Figure 9, Al experienced much larger plastic deformation than the Al with HEA coating. Therefore, the coefficient of friction of Al is much larger than that of Al with HEA coating. HEA coating significantly improves the tribological properties and reduces the wear volume loss compared to Al.

4. Conclusions

In this work, an improved molecular dynamics model has been successfully developed to simulate the mechanical and tribological properties for both pure Al and HEA coated Al. The major conclusions are summarized as follows.

1. The model shows that in the interface region between the HEA coating and Al substrate, as the laser heating temperature increases during the HEA coating additive manufacturing process, more Al in the substrate is melted to react with other elements in the coating layer. Therefore, less BCC structure (HEA phase) and more other structures (intermetallic phases) are formed. The modeling results follow the same trend reported as the experiment in Ref. [14]. Both our modeling results and experimental observation suggest that the laser heating temperature should not be too high to avoid excessive loss of the HEA phases.
2. Using the simulated nanoindentation tests, the calculated Young's modulus of pure Al and Al with HEA coating is 79.93 GPa and 119.30 GPa, respectively. In both our simulations and the experimental results in Ref. [14], the hardness of Al with the HEA coating layer is about 10 times higher than the Al hardness, indicating that HEA can significantly improve the hardness of the metallic substrate.
3. The deformations due to nanoindentation at the maximum indentation depth and after the retraction process were simulated. The HEA coated Al shows less indentation mark and smoother surface than those of the Al, which is due to the high Young's modulus and hardness of the HEA layer.
4. Using the simulated tribological scratch tests, the computed wear tracks are qualitatively in agreement with experimental images in Ref. [14]. Both our model and experiment show that the Al with HEA coating has a much smaller wear track than that of Al. The calculated

wear volume loss of Al with HEA coating (38,673 $Å^3$) is smaller than Al (1,845 $Å^3$), due to less plastic deformation, confirmed by a dislocation analysis.

5. The computed average coefficient of friction of Al is 0.62 and Al with HEA coating is 0.14. The HEA coating improves the mechanical and tribology properties, which are in good agreement with the experiments reported in Ref. [14].

Acknowledgments

This work is partially supported by the "Human Resources Program in Energy Technology (No. 20194030202450)" and "Power Generation & Electricity Delivery grant (No. 20181110100310)" of the Korea Institute of Energy Technology Evaluation and Planning (KETEP), and the National Research Foundation of Korea(NRF) grant funded by the Korea government (MSIP) (2018R1A5A6075959).

References

[1] J.-P. Couzinié, O. Senkov, D. Miracle, and G. Dirras, "Comprehensive data compilation on the mechanical properties of refractory high-entropy alloys," *Data in brief,* vol. 21, pp. 1622-1641, 2018.

[2] H. Diao, R. Feng, K. A. Dahmen, and P. Liaw, "Fundamental deformation behavior in high-entropy alloys: An overview," *Current Opinion in Solid State and Materials Science,* vol. 21, no. 5, pp. 252-266, 2017.

[3] R. Kozak, A. Sologubenko, and W. Steurer, "Single-phase high-entropy alloys–an overview," *Zeitschrift für Kristallographie-Crystalline Materials,* vol. 230, no. 1, pp. 55-68, 2015.

[4] Y. Zhou, Y. Zhang, Y. Wang, and G. Chen, "Solid solution alloys of Al Co Cr Fe Ni Ti x with excellent room-temperature mechanical properties," *Applied physics letters,* vol. 90, no. 18, p. 181904, 2007.

[5] M.-R. Chen, S.-J. Lin, J.-W. Yeh, S.-K. Chen, Y.-S. Huang, and C.-P. Tu, "Microstructure and properties of Al0. 5CoCrCuFeNiTix (x= 0–2.0) high-entropy alloys," *Materials Transactions,* vol. 47, no. 5, pp. 1395-1401, 2006.

[6] O. N. Senkov, G. Wilks, J. Scott, and D. B. Miracle, "Mechanical properties of Nb25Mo25Ta25W25 and V20Nb20Mo20Ta20W20 refractory high entropy alloys," *Intermetallics,* vol. 19, no. 5, pp. 698-706, 2011.

[7] K. M. Youssef, A. J. Zaddach, C. Niu, D. L. Irving, and C. C. Koch, "A novel low-density, high-hardness, high-entropy alloy with close-packed single-phase nanocrystalline structures," *Materials Research Letters,* vol. 3, no. 2, pp. 95-99, 2015.

[8] M. A. Hemphill *et al.*, "Fatigue behavior of Al0.5CoCrCuFeNi high entropy alloys," *Acta Materialia,* vol. 60, no. 16, pp. 5723-5734, 2012/09/01/ 2012.

[9] Y.-J. Hsu, W.-C. Chiang, and J.-K. Wu, "Corrosion behavior of FeCoNiCrCux high-entropy alloys in 3.5% sodium chloride solution," *Materials Chemistry and Physics,* vol. 92, no. 1, pp. 112-117, 2005.

[10] Y. Chen, T. Duval, U. Hung, J. Yeh, and H. Shih, "Microstructure and electrochemical properties of high entropy alloys—a comparison with type-304 stainless steel," *Corrosion science,* vol. 47, no. 9, pp. 2257-2279, 2005.

[11] C. Huang, Y. Zhang, R. Vilar, and J. Shen, "Dry sliding wear behavior of laser clad TiVCrAlSi high entropy alloy coatings on Ti–6Al–4V substrate," *Materials & Design,* vol. 41, pp. 338-343, 2012.

[12] S. Zhang, C. Wu, C. Zhang, M. Guan, and J. Tan, "Laser surface alloying of FeCoCrAlNi high-entropy alloy on 304 stainless steel to enhance corrosion and cavitation erosion resistance," *Optics & Laser Technology,* vol. 84, pp. 23-31, 2016.

[13] G. Jin *et al.*, "High temperature wear performance of laser-cladded FeNiCoAlCu high-entropy alloy coating," *Applied Surface Science,* vol. 445, pp. 113-122, 2018.

[14] G. R. Argade, S. S. Joshi, A. V. Ayyagari, S. Mukherjee, R. S. Mishra, and N. B. Dahotre, "Tribocorrosion performance of laser additively processed high-entropy alloy coatings on aluminum," *Applied Physics A,* vol. 125, no. 4, p. 272, 2019.

[15] Y. Lederer, C. Toher, K. S. Vecchio, and S. Curtarolo, "The search for high entropy alloys: a high-throughput ab-initio approach," *Acta Materialia,* vol. 159, pp. 364-383, 2018.

[16] Q. Jie, A. Cheung, and S. J. Poon, "High Entropy Alloys Mined From Phase Diagrams," *arXiv preprint arXiv:1904.08880,* 2019.

[17] Y. Ikeda, B. Grabowski, and F. Körmann, "Ab initio phase stabilities and mechanical properties of multicomponent alloys: A comprehensive review for high entropy alloys and compositionally complex alloys," *Materials Characterization,* vol. 147, pp. 464-511, 2019/01/01/ 2019.

[18] W.-M. Choi, Y. H. Jo, S. S. Sohn, S. Lee, and B.-J. Lee, "Understanding the physical metallurgy of the CoCrFeMnNi high-entropy alloy: an atomistic simulation study," *npj Computational Materials,* vol. 4, no. 1, p. 1, 2018/01/10 2018.

[19] F. Zhang, C. Zhang, S. L. Chen, J. Zhu, W. S. Cao, and U. R. Kattner, "An understanding of high entropy alloys from phase diagram calculations," *Calphad,* vol. 45, pp. 1-10, 2014/06/01/ 2014.

[20] S. Plimpton, "Fast parallel algorithms for short-range molecular dynamics," Sandia National Labs., Albuquerque, NM (United States)1993.

[21] M. S. Daw and M. I. Baskes, "Embedded-atom method: Derivation and application to impurities, surfaces, and other defects in metals," *Physical Review B,* vol. 29, no. 12, p. 6443, 1984.

[22] X. Zhou, R. Johnson, and H. Wadley, "Misfit-energy-increasing dislocations in vapor-deposited CoFe/NiFe multilayers," *Physical Review B,* vol. 69, no. 14, p. 144113, 2004.

[23] G. Anand, R. Goodall, and C. L. Freeman, "Role of configurational entropy in body-centred cubic or face-centred cubic phase formation in high entropy alloys," *Scripta Materialia,* vol. 124, pp. 90-94, 2016.

[24] Z. Lin, R. A. Johnson, and L. V. Zhigilei, "Computational study of the generation of crystal defects in a bcc metal target irradiated by short laser pulses," *Physical Review B,* vol. 77, no. 21, p. 214108, 2008.

[25] E. Yoffe, "Modified Hertz theory for spherical indentation," *Philosophical Magazine A,* vol. 50, no. 6, pp. 813-828, 1984.

[26] H. Zhao, C. Shi, P. Zhang, L. Zhang, H. Huang, and J. Yan, "Research on the effects of machining-induced subsurface damages on mono-crystalline silicon via molecular dynamics simulation," *Applied surface science,* vol. 259, pp. 66-71, 2012.

[27] A. Stukowski, "Visualization and analysis of atomistic simulation data with OVITO–the Open Visualization Tool," *Modelling and Simulation in Materials Science and Engineering,* vol. 18, no. 1, p. 015012, 2009.

[28] S. Praveen, A. Anupam, T. Sirasani, B. Murty, and R. S. Kottada, "Characterization of oxide dispersed AlCoCrFe high entropy alloy synthesized by mechanical alloying and spark plasma sintering," *Transactions of the Indian Institute of Metals,* vol. 66, no. 4, pp. 369-373, 2013.